Coordinate Control of Grid Power, Battery SoC and LVRT Protection in Single VSC Tied DFIG

Ravulakari Kalyan, Venkatakirthiga Murali* and Raja Pitchaimuthu

Department of Electrical and Electronics Engineering, National Institute of Technology, Tiruchirapalli, Tamil Nadu, India
E-mail: 407116002@nitt.edu; mvkirthiga@nitt.edu; praja@nitt.edu
**Corresponding Author*

Received 31 July 2021; Accepted 02 November 2021;
Publication 16 February 2022

Abstract

This paper proposes a coordinate control scheme for the single VSC tied doubly-fed induction generator (DFIG). In this control scheme, both the grid power and battery SoC (State of Charge) are maintained to provide an uninterrupted power supply. During the continuous operation of DFIG in the sub synchronous region, there is scope for complete battery discharge. Hence to overcome this drawback, the coordinated control scheme maintains the battery SoC level within the limits. If the SoC falls below the specified lower limit, then the proposed scheme curtails the grid power. Instead of discharging the battery, the control shifts the battery to charging mode until the safe limit of SoC is attained. During the continuous operation of DFIG in the super synchronous region, if the SoC reaches its upper limit, the proposed scheme discharges the extra power to the dump load. Further, this control scheme also introduces the low voltage ride through (LVRT) aspect according to IEGC (Indian electricity grid code) of 15% of nominal voltage and also

Distributed Generation & Alternative Energy Journal, Vol. 37_3, 587–608.
doi: 10.13052/dgaej2156-3306.37310

an enhanced rotor position computation is implemented for the effective estimation of rotor position for single VSC tied DFIG. This control makes the topology more robust and improves the reliability of the system. The proposed scheme is validated for a test system of 3.7 kW Wound Rotor Induction Machine based DG unit and investigations are done in MATLAB simulation.

Keywords: Sensor less rotor position computation (SLRPC), state of charge (SoC), voltage source converter (VSC).

1 Introduction

Nowadays renewable energy resources have become the key electric power producers, in view of limiting the usage of fossil fuels. The depletion of conventional energy sources and other environmental factors cause a drastic improvement in renewable energy sources. The wind energy conversion systems are the major production of power in renewable energy sources. There are many topologies that incorporate synchronous generators, permanent magnet synchronous generators, induction generators, and brushless DC machines. Initially, the fixed-speed machines were widely used in electric power production [1–3]. Later, thanks to development in power electronics has given helped variable speed machines to develop to next level. The doubly-fed induction machines are more suitable for WECS due to the variable nature of wind and also for reduced capacity of converters [4–6]. Many researchers have proposed the conventional type of DFIG for the control of wind power and to maintain unity power factor, which possess VSCs, where one is for control of grid power and the other is for control of voltage and reactive power support. Many control topologies viz., vector control, direct power control, and sliding mode control have been adopted for control of conventional DFIG [7–10]. Due to delays in getting the position of the rotor, the sensor less topologies got evolved [11–13]. Later, scope for research with the use of single converter for DFIG which is more economical and of reduced losses, started increasing. Hence, instead of using the grid side converter, rotor side converter connected to battery storage, was adopted to maintain the reactive power support for the system. Various control schemes are proposed for control of the single VSC – based DFIGs [14–17]. The independent control of real and reactive power of DFIG without affecting the machine parameters was proposed in [14]. In [15] the direct power control of DFIG by using rotor position estimation is explained and the same

author proposed vector control DFIG by using model reference adaptive system [16]. The algorithm proposed in [15], was adapted and improved as Rotor Position Estimation Algorithm (RPEA) in [17], and also a vector control scheme, utilizing reduced number of sensors was proposed [17]. In the above four control schemes, the SoC of battery has not been investigated in detail.

At this juncture, the authors in this paper have attempted a novel methodology, to avoid the battery getting drained out at certain critical operating conditions. In this methodology, if the machine runs less than synchronous speed the battery gets discharged, and if it is more than synchronous speed the battery gets charged. When the machine operates at the sub-synchronous region, for a longer period, and if the battery SoC reaches its minimum limit then the proposed coordinated direct power control regulates the flow of grid power, in such a way that the machine rotor is sped above synchronous speed to enable the battery charging without violating the safe limit of SoC. On the other hand, if the machine operates at super synchronous region, and if the SoC of the battery reaches the maximum limit, then the proposed direct power control re-directs the excess power to temporary (dump) loads. If the battery SoC is within the minimum and maximum permissible limits, then the proposed control regulates the generated power to the grid, according to wind velocity. The topology also proposes an improved sensorless rotor position computation (SLRPC) that helps to improve the power quality.

Besides, many researchers had earlier thrown emphasis on vector control scheme with Low Voltage Ride Through (LVRT) for conventional DFIG systems but rarely did focus on LVRT for Direct Power Control(DPC) for conventional as well as single VSC based DFIG systems [18–21]. In this regard, the authors have also attempted in this paper, a suitable methodology for counteracting all the requirements namely violation of stator currents, rotor currents, grid power, and speed of the rotor, through LVRT control for DPC upon Single VSC DFIG systems. The crowbar is connected to the rotor to safeguard the rotor side converter and battery and also the IEGC standards are validated for the power quality issues.

The rest of the paper is formulated as : Section 2 explains the coordinated power control of the single VSC tied DFIG, Section 3 explains the direct power control scheme and proposed SLRPC and Section 4 explains the coordinated power control of grid power and battery SoC. Section 5 explains the LVRT aspect of the control scheme. Section 6 presents the results and discussions for the proposed control, followed by the conclusion in Section 7.

2 Coordinated Direct Power Control of Single VSC Tied DFIG

The proposed system configuration is shown in Figure 1. It represents the wind turbine that drives the induction machine connected to the grid and the rotor is connected to battery storage through VSC. The control consists of a coordinated power control block controlled through the direct power control scheme which gives appropriate gate pulses to VSC.

2.1 Wind Turbine Design

A 6.5 kw wind turbine is coupled to a 3.7 kW slip-ring/wound-rotor induction machine. The machine base speed is chosen as 12 m/s. The pitch angle of the turbine (β) is zero. The wind turbine output power (P_w) is given by

$$P_w = 0.5\rho A V_\omega^3 C_p(\lambda, \beta) \tag{1}$$

where the parameters are: rho (ρ) represents air density is 1.225 kg/m^3, swept area (A) in m^2, wind turbine velocity (V_W) in m/s, and power coefficient (Cp) calculated by using tip speed ratio (λ) and β which is given in [15].

$$C_p(\lambda, \beta) = C_1 \left\{ \left(\frac{C_2}{\lambda_i} \right) - C_3\beta - C_4 \right\} e^{\frac{C_5}{\lambda_i}} + C_6\lambda \tag{2}$$

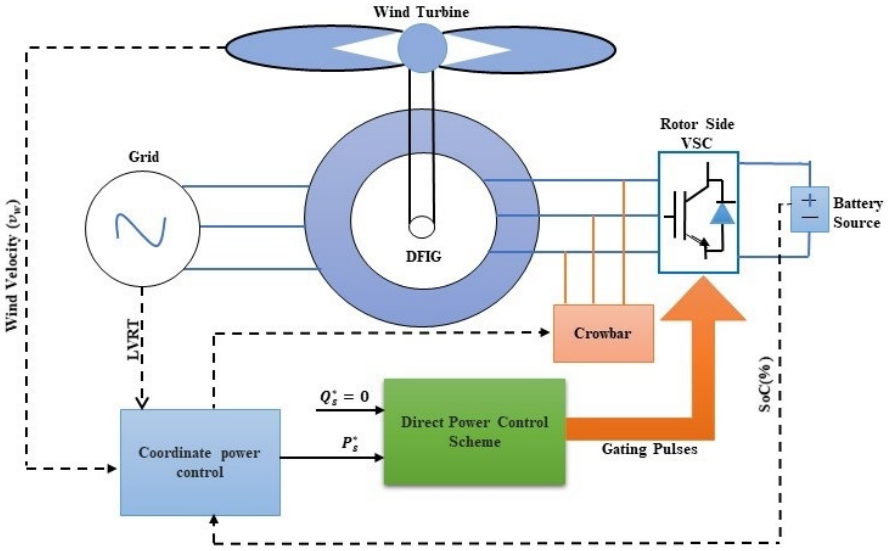

Figure 1 Topology of coordinated control for single VSC tied DFIG.

where $\frac{1}{\lambda_i} = \{\frac{1}{1+C_7\beta}\} - \{\frac{C_8}{\beta^3+1}\}$, $C_1 = 0.5176$, $C_2 = 116$, $C_3 = 0.4$, $C_4 = 5$, $C_5 = 21$, $C_6 = 0.0068$, $C_7 = 0.08$, and $C_8 = 1$.

The tip speed ratio (λ) is given as

$$\lambda = \frac{\omega R}{V_\omega} \tag{3}$$

where ω is the rotation speed of generator in rad/s and R is the radius of blade swept area in meter (m).

2.2 Determination of Battery Voltage

The machine is operated at a speed between 0.7 p.u. to 1.3 p.u. and the battery voltage is selected as two times the maximum peak rotor voltage. Therefore, the maximum possible rotor voltage per phase (V_r) is computed as

$$V_r = S_{max}\frac{V_L}{\sqrt{3}}\frac{N_r}{N_s} \tag{4}$$

where S_{max} is maximum slip which is taken as 0.3, V_L is line voltage which is taken as 415 V and N_r/N_s is rotor to stator turns ratio which is 1/2. Then the computed rotor voltage per phase is 35.94 V.

The dc-link voltage (V_{dc}) is computed as

$$V_{dc} \geq \frac{2\sqrt{2}}{m}V_r \tag{5}$$

where the modulation index is taken as 1 and the value of $\mathrm{V_{dc}}$ should be greater than 101.65 V with respect to Equation (5). As per standards, the battery voltage is selected as 240 V [15].

3 The Direct Power Control Scheme

The control schematic of direct power control is shown in Figure 2. In this control scheme, the real and reactive powers are controlled through two 3L (3-level) HC (hysteresis control) controllers as shown in Figure 2. The errors(P_{ER}, Q_{ER}) for the HC controllers are obtained from stator real and reactive powers (P_S, Q_S) obtained from stator voltage and current quantities and reference real and reactive powers (P_S^*, Q_S^*). The reference real power is obtained based on the wind velocity and reference reactive power is chosen as zero in order to ascertain the unity power factor.

$$P_{ER} = P_S^* - P_S, \quad Q_{ER} = Q_S^* - Q_S \tag{6}$$

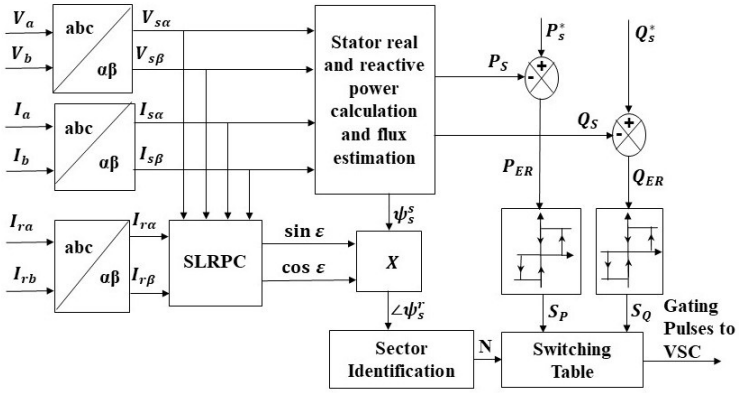

Figure 2 Direct power control for single VSC tied DFIG.

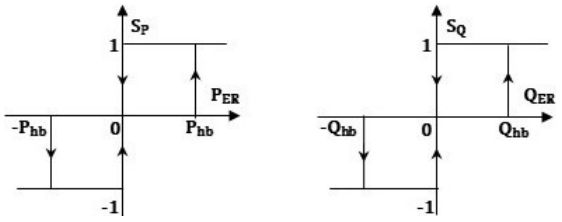

Figure 3 HC controllers for real power and reactive power.

The actual real and reactive powers are computed as

$$P_S = 3/2(V_{s\alpha}I_{s\alpha} + V_{s\beta}I_{s\beta}), \quad Q_S = 3/2(V_{s\beta}I_{s\alpha} - V_{s\alpha}I_{s\beta}) \tag{7}$$

where the stator voltage and current quantities are computed as

$$V_{s\alpha} = 3/2\, V_{sa} \quad \text{and} \quad I_{s\alpha} = 3/2\, I_{sa} \tag{8}$$

$$V_{s\beta} = \sqrt{3}/2\, (V_{sa} + 2V_{sb}) \quad \text{and} \quad I_{s\beta} = \sqrt{3}/2\, (I_{sa} + 2I_{sb}) \tag{9}$$

3.1 HC Control Scheme

The errors from comparators are given to the HC controllers which generate the switching states (S_P, S_Q) and P_{hb} and Q_{hb} are hysteresis bands for controllers respectively shown in Figure 3.

The switching states from both HC controllers are as follows

$$\mathrm{S}_P = 1, \quad \text{when } \mathrm{P}_{ER} > \mathrm{P}_{\mathrm{hb}} \tag{10}$$

$$\mathrm{S}_P = -1, \quad \text{when } \mathrm{P}_{ER} < -\mathrm{P}_{\mathrm{hb}} \tag{11}$$

$$\mathrm{S}_P = 0, \quad \text{when } -\mathrm{P}_{\mathrm{hb}} < \mathrm{P}_{ER} < \mathrm{P}_{\mathrm{hb}} \tag{12}$$

$$\mathrm{S}_Q = 1, \quad \text{when } \mathrm{Q}_{ER} > \mathrm{Q}_{\mathrm{hb}} \tag{13}$$

$$\mathrm{S}_Q = -1, \quad \text{when } \mathrm{Q}_{ER} < -\mathrm{Q}_{\mathrm{hb}} \tag{14}$$

$$\mathrm{S}_Q = 0, \quad \text{when } -\mathrm{Q}_{\mathrm{hb}} < \mathrm{Q}_{ER} < \mathrm{Q}_{\mathrm{hb}} \tag{15}$$

3.2 Sensor Less Rotor Position Computation (SLRPC)

The computation of rotor position is obtained from SLRPC and the parameters required are stator voltages ($V_{s\alpha}, V_{s\beta}$), stator currents ($I_{s\alpha}, I_{s\beta}$) and rotor currents ($I_{r\alpha}, I_{r\beta}$). Figure 4 shows the SLRPC schematic diagram and the stator quantities are explained earlier and the rotor current components are given in Equations (16) and (17).

$$I_{r\alpha} = 3/2\ I_{ra} \tag{16}$$

$$I_{r\beta} = \sqrt{3}/2\ (I_{ra} + 2I_{rb}) \tag{17}$$

Here, the rotor position computation obtained in a direct approach and stator voltage angle aligned with Q-axis i.e., $V_s = V_q$ and $V_d = 0$ respectively.

According to reference frame theory the rotor position is obtained from Figure 5. The angle θ_S is the angle between stator voltage (V_S) and stator reference frame, I_r makes an angle θ_x with respect to stator reference frame (S.R.F.) and θ_y with rotor reference frame (R.R.F.). Hence, the slip angle ε is obtained from θ_x and θ_y.

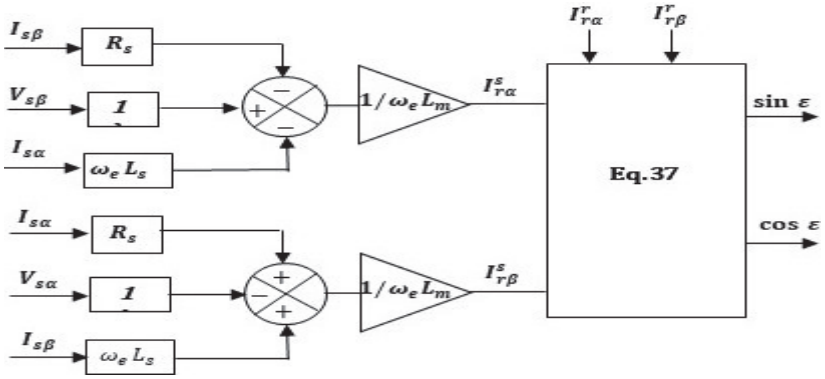

Figure 4 SLRPC computation for slip angle vectors.

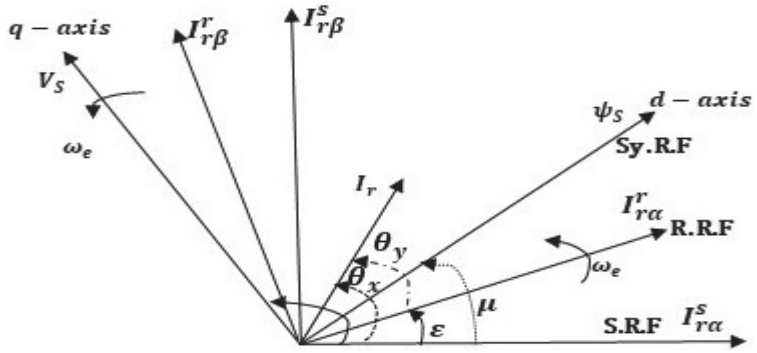

Figure 5 Phasor representation of vectors in respective reference frames.

The flux linkage equations of the stator in the stator reference frame are given as

$$\psi_{s\alpha} = L_s I_{s\alpha} + L_m I_{r\alpha} \tag{18}$$

$$\psi_{s\beta} = L_s I_{s\beta} + L_m I_{r\beta} \tag{19}$$

The rotor currents from the above equations in the stator reference frame are computed as

$$I_{r\alpha} = \frac{\psi_{s\alpha} - L_s I_{s\alpha}}{L_m} \tag{20}$$

$$I_{r\beta} = \frac{\psi_{s\beta} - L_s I_{s\beta}}{L_m} \tag{21}$$

The flux linkage terms from the machine voltage equations are expressed as

$$V_{s\alpha} = R_s I_{s\alpha} + \frac{d}{dt}\psi_{s\alpha} \tag{22}$$

$$V_{s\beta} = R_s I_{s\beta} + \frac{d}{dt}\psi_{s\beta} \tag{23}$$

The components of stator flux in the stator reference frame is expressed in terms of stator magnetizing components along the d-axis in the synchronous reference frame (Sy. R. F.) computed as

$$\psi_{\mathrm{s}\alpha} = |\psi_{\mathrm{s}}|\cos(\mu) \tag{24}$$

$$\psi_{\mathrm{s}\beta} = |\psi_{\mathrm{s}}|\sin(\mu) \tag{25}$$

On differentiation, the above equations being functions of time, become:

$$\frac{\mathrm{d}}{\mathrm{dt}}\psi_{\mathrm{s}\alpha} = \frac{\mathrm{d}}{\mathrm{dt}}|\psi_{\mathrm{s}}|\sin(\mu) - \psi_{\mathrm{s}\beta}(\omega_{\mathrm{e}}) \tag{26}$$

$$\frac{\mathrm{d}}{\mathrm{dt}}\psi_{\mathrm{s}\beta} = \frac{\mathrm{d}}{\mathrm{dt}}|\psi_{\mathrm{s}}|\cos(\mu) + \psi_{\mathrm{s}\alpha}(\omega_{\mathrm{e}}) \tag{27}$$

where $\omega_{\mathrm{e}} = \frac{\mathrm{d}(\mu)}{\mathrm{dt}}$ is the angular velocity of stator flux. In the above equation, the magnitude of differentiating total magnetizing flux linkages is negligible. So, the respective stator voltage equations are computed as follows

$$\mathrm{V}_{\mathrm{s}\alpha} = \mathrm{R}_{\mathrm{s}}\mathrm{I}_{\mathrm{s}\alpha} - \mathrm{L}_{\mathrm{s}}I_{\mathrm{s}\beta}\omega_{\mathrm{e}} - \mathrm{L}_{\mathrm{m}}I_{\mathrm{r}\beta}\omega_{\mathrm{e}} \tag{28}$$

$$V_{\mathrm{s}\beta} = \mathrm{R}_{\mathrm{s}}I_{\mathrm{s}\beta} + \mathrm{L}_{\mathrm{s}}I_{\mathrm{s}\alpha}\omega_{\mathrm{e}} + \mathrm{L}_{\mathrm{m}}\mathrm{I}_{\mathrm{r}\alpha}\omega_{\mathrm{e}} \tag{29}$$

The rotor currents in the stator reference frame from the above equations are computed as follows

$$I^{\mathrm{s}}_{\mathrm{r}\alpha} = \frac{V_{\mathrm{s}\beta} - \mathrm{R}_{\mathrm{s}}I_{\mathrm{s}\beta} - \mathrm{L}_{\mathrm{s}}I_{\mathrm{s}\alpha}\omega_{\mathrm{e}}}{\omega_{\mathrm{e}}\mathrm{L}_{\mathrm{m}}} \tag{30}$$

$$I^{s}_{\mathrm{r}\beta} = \frac{\mathrm{R}_{\mathrm{s}}I_{\mathrm{s}\alpha} - V_{\mathrm{s}\alpha} + \omega_{\mathrm{e}}\mathrm{L}_{\mathrm{s}}I_{\mathrm{s}\beta}}{\omega_{\mathrm{e}}\mathrm{L}_{\mathrm{m}}} \tag{31}$$

The only unknown term from the above equations is stator angular velocity (ω_{e}) which is identified by using stator quantities ($V_{\mathrm{s}\alpha}$, $V_{\mathrm{s}\beta}$) in stator reference frame computed as

$$\sin(\mu) = -\mathrm{V}_{\mathrm{s}\alpha}/\sqrt{V^2_{\mathrm{s}\alpha} + V^2_{\mathrm{s}\beta}} \tag{32}$$

$$\cos(\mu) = V_{\mathrm{s}\beta}/\sqrt{V^2_{\mathrm{s}\alpha} + V^2_{\mathrm{s}\beta}} \tag{33}$$

Hence,

$$\omega_{\mathrm{e}} = \cos(\mu)\frac{\mathrm{d}}{\mathrm{dt}}\sin(\mu) - \sin(\mu)\frac{\mathrm{d}}{\mathrm{dt}}\cos(\mu) \tag{34}$$

The relation between rotor currents in the stator reference frame and rotor reference frame is given as

$$I_{\mathrm{r}\alpha} + \mathrm{j}I_{\mathrm{r}\beta} = (\mathrm{I}^{\mathrm{s}}_{\mathrm{r}\alpha} + \mathrm{j}I^{\mathrm{s}}_{\mathrm{r}\beta})\mathrm{e}^{\mathrm{j}(\theta_x - \theta_y)} \tag{35}$$

$$\begin{bmatrix} I_{\mathrm{r}\alpha} \\ I_{\mathrm{r}\beta} \end{bmatrix} = \begin{bmatrix} I^{\mathrm{s}}_{\mathrm{r}\alpha} & -I^{\mathrm{s}}_{\mathrm{r}\beta} \\ I^{\mathrm{s}}_{\mathrm{r}\beta} & I^{\mathrm{s}}_{\mathrm{r}\alpha} \end{bmatrix} \begin{bmatrix} \cos(\varepsilon) \\ \sin(\varepsilon) \end{bmatrix} \tag{36}$$

The slip angle equations are computed as ($\varepsilon = \theta_x - \theta_y$)

$$\begin{bmatrix}\cos(\varepsilon)\\ \sin(\varepsilon)\end{bmatrix} = \begin{bmatrix}\dfrac{I^{\mathrm{s}}_{\mathrm{r}\alpha} I_{\mathrm{r}\alpha} + I^{\mathrm{s}}_{\mathrm{r}\beta} I_{\mathrm{r}\beta}}{(I^{\mathrm{s}}_{\mathrm{r}\alpha})^2 + (I^{\mathrm{s}}_{\mathrm{r}\beta})^2}\\ \dfrac{-I^{\mathrm{s}}_{\mathrm{r}\beta} I_{\mathrm{r}\alpha} + I^{\mathrm{s}}_{\mathrm{r}\alpha} I_{\mathrm{r}\beta}}{(I^{\mathrm{s}}_{\mathrm{r}\alpha})^2 + (I^{\mathrm{s}}_{\mathrm{r}\beta})^2}\end{bmatrix} \tag{37}$$

The required stator flux in the rotor reference frame is computed as

$$\psi^{\mathrm{r}}_{\mathrm{s}} = (\psi_{\mathrm{s}\alpha} + \mathrm{j}\psi_{\mathrm{s}\beta})(\cos(\varepsilon) + \mathrm{j}\,\sin(\varepsilon)) \tag{38}$$

where the stator flux components in the stator reference frame computed as

$$\psi_{\mathrm{s}\alpha} = \int (V_{\mathrm{s}\alpha} - \mathrm{R_s} I_{\mathrm{s}\alpha})\mathrm{dt} \tag{39}$$

$$\psi_{\mathrm{s}\beta} = \int (V_{\mathrm{s}\beta} - \mathrm{R_s} I_{\mathrm{s}\beta})\mathrm{dt} \tag{40}$$

The position is acquired from stator flux in the rotor reference frame, which is used to generate sector location (N) in the space vector, as shown in Figure 6. The sector location and the switching states from the HC controllers, are used to generate voltage vectors for the VSC. The voltage vectors are 6 active ($V_1 - V_6$) and 2 zero vectors (V_0, V_7) respectively. The voltage vectors are $V_0(000) - V_7(111)$, the inner binary digits are the gate pulses for upper case switches for the 6-pulse VSC and for the bottom switches takes the opposite pulses and vice versa. The '0' indicates OFF and '1' indicates ON and the switching table is shown in Table 1.

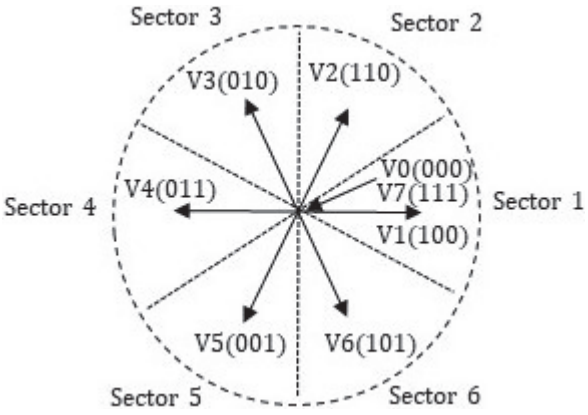

Figure 6 Sector location of voltage vectors.

Table 1 Voltage pulses for RSC with respect to sector location

S_Q	S_P	Sector 1	Sector 2	Sector 3	Sector 4	Sector 5	Sector 6
1	1	V_5	V_4	V_6	V_2	V_3	V_1
	0	V_4	V_6	V_2	V_3	V_1	V_5
	−1	V_6	V_2	V_3	V_1	V_5	V_4
0	1	V_1	V_5	V_4	V_6	V_2	V_3
	0	V_7	V_7	V_7	V_7	V_7	V_7
	−1	V_2	V_3	V_1	V_5	V_4	V_6
−1	1	V_1	V_5	V_4	V_6	V_2	V_3
	0	V_3	V_1	V_5	V_4	V_6	V_2
	−1	V_2	V_3	V_1	V_5	V_4	V_6

4 The Proposed Coordinate Power Control Scheme

In this control scheme, when the machine is under sub-synchronous operation, the battery discharges and when the machine is under the super synchronous operation, the battery charges. Power fed to the grid, is based on the respective wind velocity. Besides, the SoC is controlled according to its minimum and maximum specified limits. If the machine is continuously in the sub-synchronous region, and if the SoC is less than the minimum limit, then the control schemes regulate the grid power such that the machine runs above synchronous speed. Hence, the battery shifts to the charging mode and it charges up to the safer limit of SoC. If the machine operates in super synchronous region, for a longer duration and also the battery continued in charging mode, there is always a chance for the SoC to reach its maximum limit. Then the control sends the excess power to the dump load. The coordinated power control flow chart is to understand the coordination between the battery SoC and grid power as shown in the Figure 7.

There are three conditions considered in the flow chart, viz., the machine operated at the synchronous speed of 10 m/s, less than 10 m/s for sub synchronous speed and greater than 10 m/s for super synchronous speed. Further the control is coordinated with battery SoC limits with respect to wind speed such that grid power is controlled according to the percentage of SoC.

5 LVRT Aspect for Single VSC Tied DFIG

In this control scheme, the crowbar is connected when the LVRT occurs for a specific period of time to safeguard the rotor side converter. As per IEGC standards, the low voltage ride-through is shown in Figure 8.

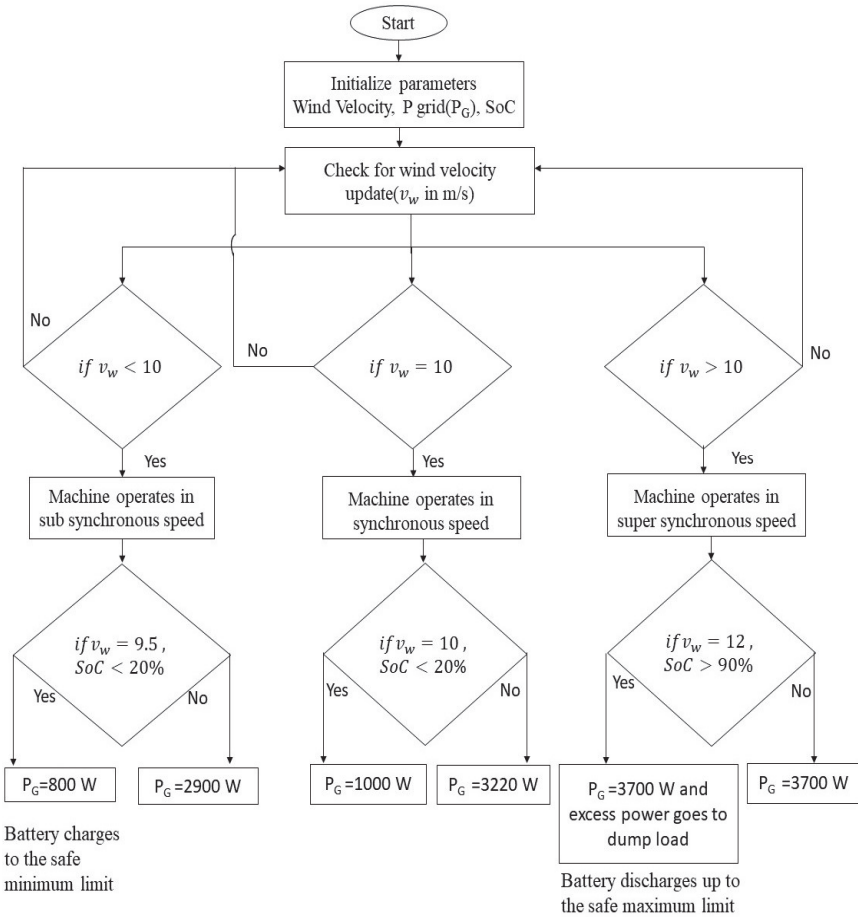

Figure 7 Flow chart of the proposed coordinated control scheme.

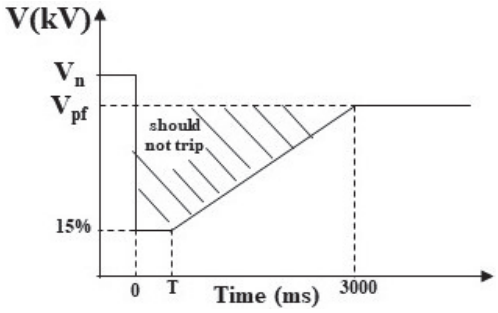

Figure 8 IEGC standard for LVRT.

Where V_n is the nominal voltage, V_{pf} is the 80% of nominal voltage mentioned by IEGC, T is the fault clearing time depending upon the nominal voltage level of machines. In the shaded region, the machine should not trip so that the wind turbine could connect to the grid. Proposed control effectively protecting the rotor side converter with the crowbar low resistance path without any violations in stator current and speed of the rotor. The above standards are made for more than 33 kV and the proposed control is scaled for a voltage of 415 V.

6 Results and Discussions

parameters considered for simulation are voltages (V_{sa}, V_{sb}) and currents (I_{sa}, I_{sb}) from the stator and currents (I_{ra}, I_{rb}) from the rotor. These voltages and currents are converted into 2-phase (α, β) quantities by using Equations (8)–(9), and (17). From Equation (7) the stator real and reactive powers are calculated. The reference powers (P_s^*) are obtained from coordinated control block and (Q_s^*) is chosen as zero. The error comparator generates the error in Equation (6) which is given to 3L-HC controllers generates switching states given in Equations (10)–(15).

From the 2-phase quantities of stator and rotor, the SLRPC computation generates slip angles given in Equation (37). The stator flux quantities from Equations (39)–(40) and slip angle vectors are helpful in finding the stator flux position in the rotor reference frame. The stator flux position in the rotor reference frame is used to compute the sector location (N). The switching states (S_P, S_Q) and sector location (N) generate the gate pulses for the VSC.

The investigations are done to analyse the performance of the proposed controller and the results are shown in various operating conditions and as well as balanced operating conditions.

6.1 Normal Operating Conditions (Under SoC Limits)

Figure 9 explains the performance waveforms of DFIG under various operating speeds such as 7 m/s, 10 m/s, 12 m/s respectively. The observations from the below figure at wind velocity of 7 m/s, the machine runs up to 4 secs in the sub-synchronous region of 0.7 p.u. the sector is in the clockwise direction, the actual and computed positions are equally matched, reactive power tracking zero (u.p.f.) and the wind turbine is not able to produce the required grid power (P_S) then the battery power (P_B) discharges than the sum of both powers fed to the grid of 1650 W.

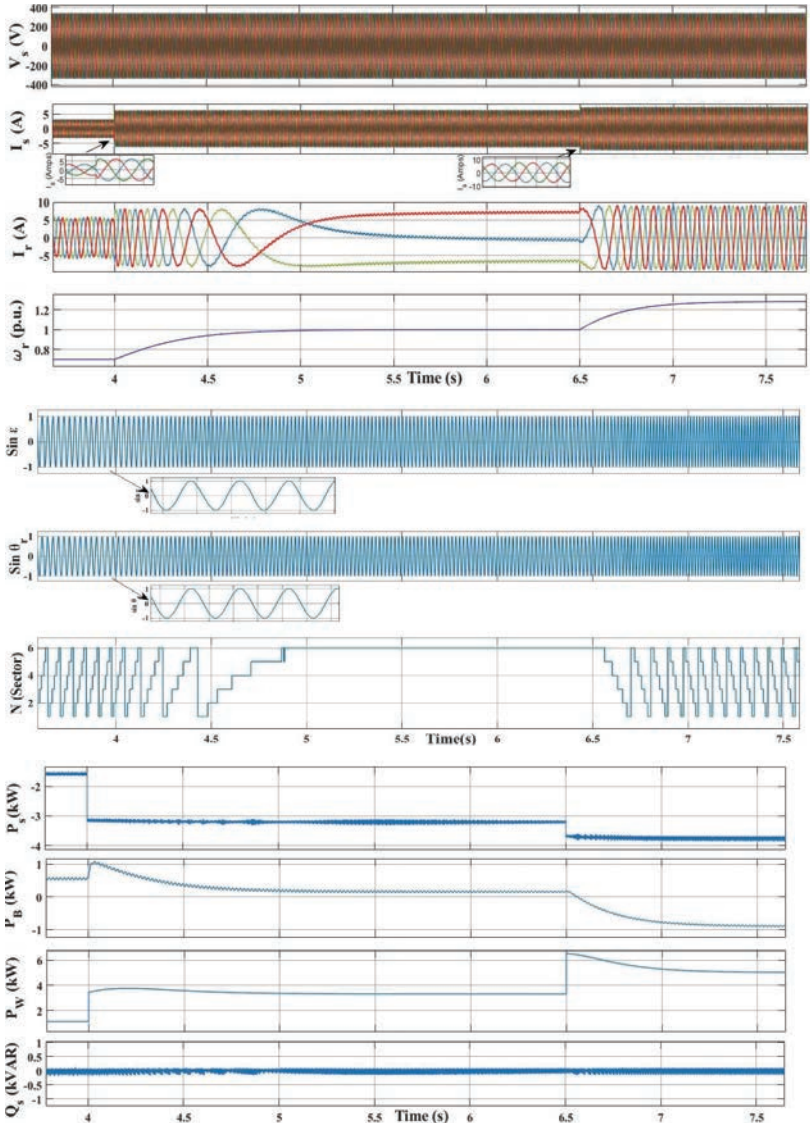

Figure 9 Performance of machine under normal operating conditions.

At 4 sec the machine runs at synchronous speed for a velocity of 10 m/s, the machine produces a power of 3220 W and the battery discharges to the losses (ideally battery neither charges nor discharges). Here, the observations from waveforms are rotor currents and sector location are steady in nature.

Table 2 Gives parameter changes at various speed conditions

Parameters \ Cases	P_S(W)	Rotor Speed (p.u.)	Rotor Current Direction	Sector	Battery Condition
Sub Synchronous Region@7m/s	1650	0.7	Normal	Clockwise	Discharge
Synchronous Region@10m/s	3220	1.0	Steady	Steady	Slight discharge to losses (ideally zero)
Super Synchronous Region@12m/s	3700	1.3	Reverse	Anti-clockwise	Charge

At 6.5 sec the machine runs at super synchronous speed for a velocity of 12 m/s, then the observations are the sector location is in the anti-clockwise direction and the rotor currents also reversed. Here, the wind turbine is able to produce more than the required power. So, the battery starts charging and the wind power (P_W) fed to the grid is 3700 W.

The summary of various machine operation conditions is given in Table 2 and the machine reactive power maintained at zero such that unity power factor maintained throughout the operation.

6.2 The Machine Under Critical Operating Conditions (SoC $<$ 20%, SoC $>$ 90%)

The proposed control makes these conditions favorable to the system as follows: Figure 10 shows the machine is operating at a speed of 9.5 m/s, the power fed to the grid of 2900 W and the battery is in discharge condition.

When the machine continuously operates under a sub synchronous region, if the battery discharges less than 20% then the proposed control curtails its grid power to charge the battery as the speed of the machine raises above synchronous speed. From the above observations, when grid power is reduced the stator current is reduced, the rotor currents change their direction as the sector changes its direction, the battery in charging mode, reactive power is zero (unity power factor). Figure 11 shows the SoC(%), initially battery is in discharged condition. when it is below 20%, the battery gets charged to a safe limit of SoC and later it follows the previous condition.

When the machine is at the synchronous speed of 10 m/s, the battery neither charges nor discharges, but practically it discharges to losses. So, the same condition is applicable for both sub synchronous and super synchronous speeds.

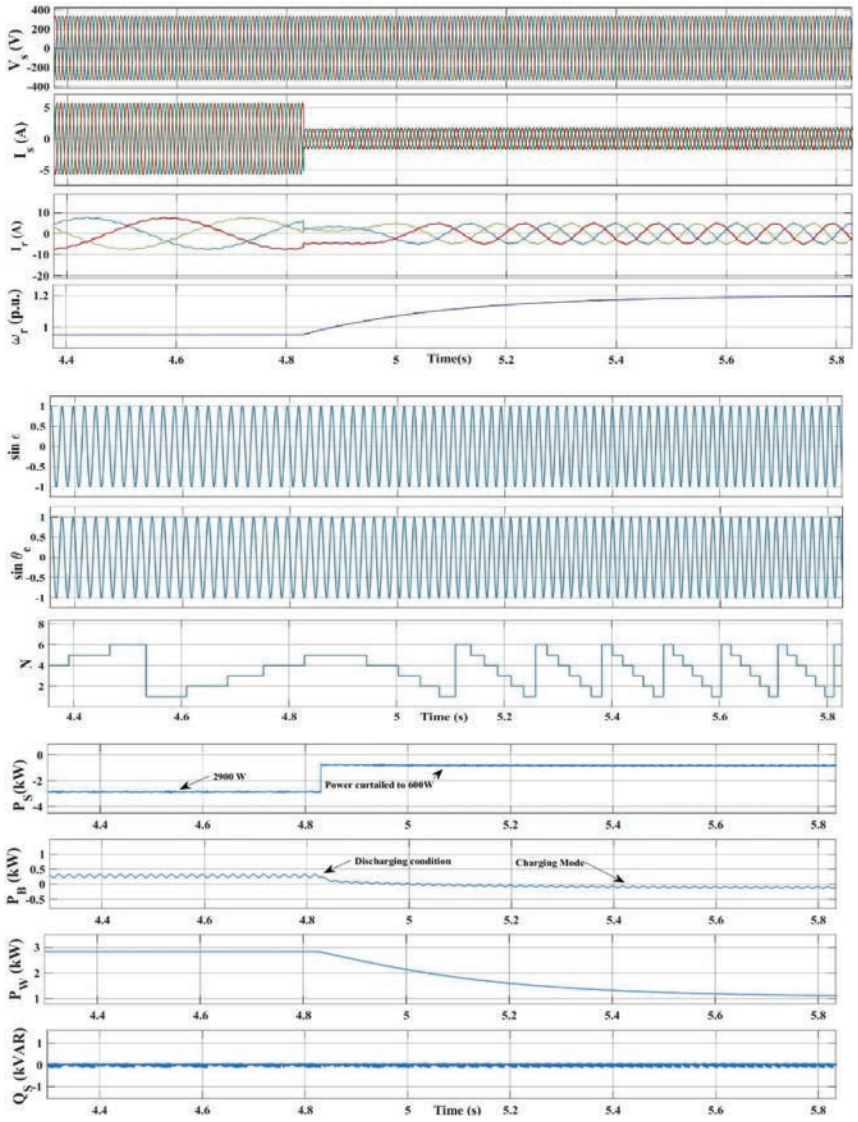

Figure 10 Performance of machine operating at a speed of 9.5 m/s and Soc $<$ 20% at 4.8 sec.

When the machine runs continuously at super synchronous region of 12 m/s, the battery charges continuously. When battery SoC becomes more than 90% the proposed control scheme activates the breaker at DC Side. Then the excess power is sent to the dump load. At this condition the

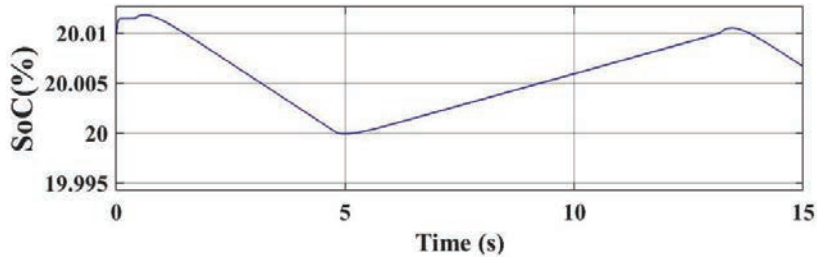

Figure 11 The machine continuously operating at a speed of 9.5 m/s (SoC $< 20\%$).

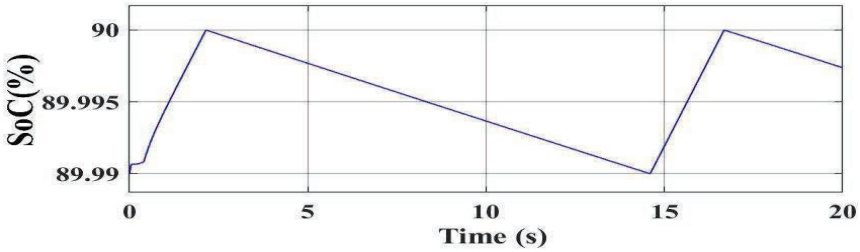

Figure 12 SoC at maximum limits under super synchronous region (SoC $> 90\%$).

machine parameters do not change, the performance waveforms are the same as the normal condition but, the change is only seen in SoC and the battery discharges to the safer limit of maximum SoC limit. Figure 12 shows the SoC when the battery source is connected to the dump load.

6.3 LVRT of 15% of the Nominal Voltage Applied According to IEGC

The LVRT occurred at the 3 to 3.5 sec in the grid supply where the grid voltage changes from maximum voltage to 15% of maximum voltage as shown in Figure 13. At 3.5 to 3.92 sec the grid voltage recovers to its rated value at the rate of 15 p.u./s.

Between 3 to 3.1 sec the crowbar is activated to avoid high inrush currents in the rotor circuit and at this condition, the rotor is connected with crowbar resistance which protects the rotor side converter shown in Figure 14. The grid power is curtailed during this period to minimum power ($P_{\min}$) such that speed and stator current cannot violate the machine-rated limits. The minimum power of 600 W is maintained till it reaches 50% of the rated voltage then it changes to rated reference power according to wind speed. Here, the machine operated at 12 m/s and the respective waveforms presented.

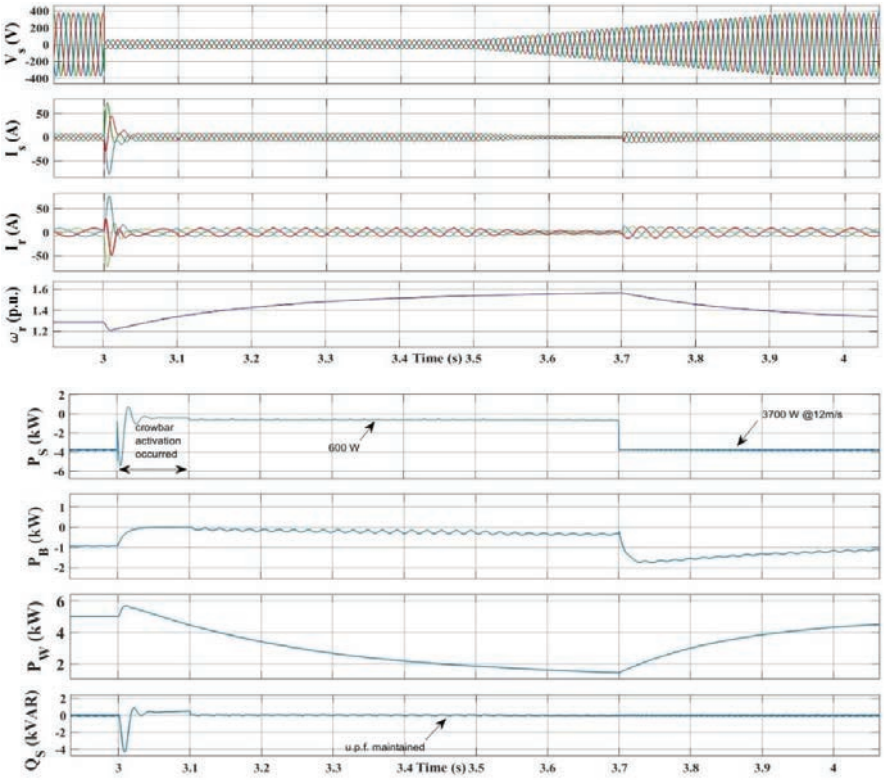

Figure 13 The changes in parameters of machine subjected to LVRT.

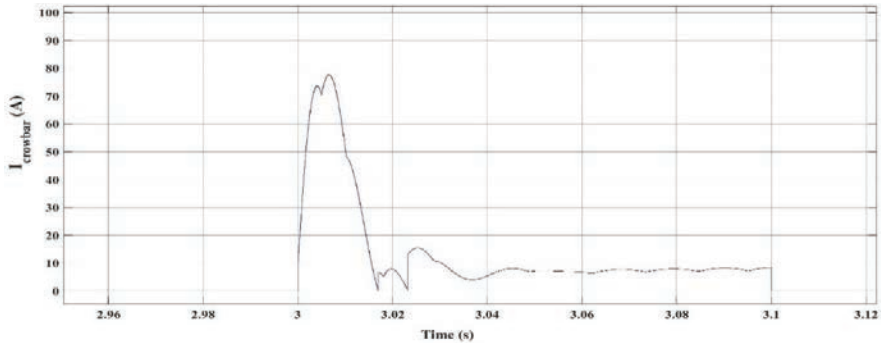

Figure 14 Current in the crowbar resistance.

7 Conclusion and Future Scope

In this paper, the authors have presented a coordinated controller for single VSC based DFIG unit to balance the grid power and battery power, in view of improved power quality and effective power balance in the system. The proposed improved coordinated power control scheme effectively maintains the power balance within the permissible minimum and maximum SoC conditions. The topology is more reliable compared to other schemes experimented earlier and also the proposed SLRPC algorithm effectively computes the position of the rotor, where the computations are independent of the machine parameters. As the proposed methodology does not require any complex calculations, on digital implementation it is expected to require less memory compared to earlier schemes discussed in the literature. The proposed LVRT scheme is a new attempt by the authors, with direct power control which effectively counteracts the undervoltage faults, on par with IEGC standards. The system is capable of operating in various speed conditions with appreciative transient response.

References

[1] R. Datta, and V.T. Ranganathan. 'Variable-speed wind power generation using doubly fed wound rotor induction machine-a comparison with alternative schemes'. IEEE Trans. On Energy Conversion 17, 414–421, 2002.

[2] L. Holdsworth, X. G. Wu, J. B. Ekanayake and N. Jenkins. 'Comparison of fixed speed and doubly-fed induction wind turbines during power system disturbances'. IEE Proc., Gener. Transm. Distrib. 150, 343, 2003.

[3] S.S. Murthy, B. Singh, P.K. Goel, and S.K. Tiwari. 'A Comparative Study of Fixed Speed and Variable Speed Wind Energy Conversion Systems Feeding the Grid'. in 2007 7th International Conference on Power Electronics and Drive Systems (Bangkok, Thailand: IEEE), 736–743.

[4] R. Pena, J.C. Clare, and G. M. Asher. 'Doubly fed induction generator using back-to-back PWM converters and its application to variable-speed wind-energy generation'. IEE Proc., Elect. Power Appl., 143, 231–241, 1996.

[5] S. Muller, M. Deicke, and R.W. De Doncker. 'Doubly fed induction generator systems for wind turbines'. IEEE Ind. Appl. Mag. 8, 26–33, 2002.

[6] A. Tapia, G. Tapia, J.X. Ostolaza, and J.R. Saenz. 'Modelling and control of a wind turbine driven doubly fed induction generator'. IEEE Trans. On Energy Conversion 18, 194–204, 2003.
[7] E. Bogalecka. 'Power control of a double fed induction generator without speed or position sensor'. in Conf. Rec. EPE, 377, 224–228, 1993.
[8] L. Xu, and P. Cartwright. 'Direct Active and Reactive Power Control of DFIG for Wind Energy Generation'. IEEE Trans. On Energy Conversion 21, 750–758, 2003.
[9] D. Zhi, and L. Xu. 'Direct Power Control of DFIG with Constant Switching Frequency and Improved Transient Performance'. IEEE Trans. On Energy Conversion 22, 110–118, 2007.
[10] J. Mohammadi, S. Vaez-Zadeh, S. Afsharnia, and E. Daryabeigi. 'A Combined Vector and Direct Power Control for DFIG-Based Wind Turbines'. IEEE Trans. Sustain. Energy 5, 767–775, 2014.
[11] R. Datta, and V.T. Ranganathan. 'Direct power control of grid-connected wound rotor induction machine without rotor position sensors. IEEE Trans. Power Electron. 16, 390–399, 2001(b).
[12] R. Datta, and V.T. Ranganathan. 'A simple position-sensor less algorithm for rotor-side field-oriented control of wound-rotor induction machine'. IEEE Trans. Ind. Electron. 48, 786–793, 2001(a).
[13] A. Karthikeyan, C. Nagamani, and G.S. Ilango. 'A Versatile Rotor Position Computation Algorithm for the Power Control of a Grid-Connected Doubly Fed Induction Generator'. IEEE Trans. Energy Convers. 27, 697–706, 2012.
[14] K. Vijayakumar, S.B. Tennakoon, N. Kumaresan, and N.G. Ammasai Gounden. 'Real and reactive power control of hybrid excited wind-driven grid-connected doubly fed induction generators'. IET Power Electronics 6, 1197–1208, 2013.
[15] B. Singh, and N. K. Swami Naidu. 'Direct Power Control of Single VSC-Based DFIG Without Rotor Position Sensor'. IEEE Trans. on Ind. Appl. 50, 4152–4163, 2014.
[16] N.K. Swami Naidu, and B. Singh. 'Sensorless control of single voltage source converter-based doubly fed induction generator for variable speed wind energy conversion system'. IET Power Electronics 7, 2996–3006, 2014.
[17] R.M. Prasad, and M.A. Mulla. 'A Novel Position-Sensorless Algorithm for Field-Oriented Control of DFIG With Reduced Current Sensors. IEEE Trans. Sustain. Energy 10, 1098–1108, 2019.

[18] G. Abad, J. Lopez, M.A. Rodriguez, M. Luis. 'Doubly Fed Induction Machine'. Hoboken, NJ, USA: John Wiley & Sons, Inc, 2011.
[19] M.A. Asha Rani, C. Nagamani, G. Saravana Ilango, A. Karthikeyan. 'An Effective Reference Generation Scheme for DFIG With Unbalanced Grid Voltage'. IEEE Trans. Sustain. Energy 5, 1010–1018, 2014.
[20] http://niwe.res.in/NIWE_OLD/Hindi/Docu/Wind_grid_code_for_Ind
[21] http://www.cercind.gov.in/2016/orders/420_mp_2014.pdf
[22] W. Leonhard. 'Control of electrical drives'. Third edition. Berlin Heidelberg: Springer, 2001.

Biographies

Ravulakari Kalyan received the bachelor's degree in Electrical and Electronics Engineering from BVRIT affiliated to JNTUH in 2010, and the master's degree in Power engineering from SICET affiliated to JNTUH in 2014 respectively. He is currently pursuing as Ph.D. Scholar (2016) at the Department of Electrical and Electronics Engineering, National Institute of Technology, Tiruchirapalli. His research areas include renewable energy sources, power converters and battery storage systems.

Venkatakirthiga Murali completed her B.E. in Electrical and Electronics Engineering and M.Tech. in Power Systems in 2000 and 2004 respectively.

She is currently working as an Associate Professor at the EEE department of the National Institute of Technology Tiruchirappalli India and has a total of eighteen years of teaching experience. She is with NITT since 2006 and has published 45 – international journal and conference publications of IEEE and Springer. She is a reviewer for many reputed journals. She has guided many UG and PG projects. She has also guided 3 Ph.D.s and 1 M.S. (by research). She is senior IEEE member and Fellow of Institution of Engineers India. Her areas of interest are Power Systems, Distributed Generation and Micro-grids and High Voltage DC Transmission.

Raja Pitchaimuthu obtained his M.Tech degree in Energy Systems from Indian Institute of Technology Madras, Chennai in 2002 and PhD degree from National Institute of Technology, Tiruchirappalli in 2013. He is presently an Associate Professor in the Department of Electrical and Electronics Engineering at National Institute of Technology, Tiruchirappalli at India where he has been since 2006. His field of interest is design and development of controllers for power converters used in solar and wind energy conversion systems. He also does research in the development of protection schemes for transmission and distribution systems. He is a Senior Member in IEEE, life member of ISTE and Institution of Engineers (India).